

---

This is an electronic reprint of the original article.  
This reprint may differ from the original in pagination and typographic detail.

Moreno, Resti Montoya; Kurvinen, Joni; Ala-Laurinaho, Juha; Khripkov, Alexander; Ilvonen, Janne; van Wonterghem, Jari; Viikari, Ville

## Dual-Polarized mm-Wave End-Fire Chain-Slot Antenna for Mobile Devices

*Published in:*  
IEEE Transactions on Antennas and Propagation

*DOI:*  
[10.1109/TAP.2020.3001434](https://doi.org/10.1109/TAP.2020.3001434)

Published: 01/01/2021

*Document Version*  
Publisher's PDF, also known as Version of record

*Published under the following license:*  
CC BY

*Please cite the original version:*  
Moreno, R. M., Kurvinen, J., Ala-Laurinaho, J., Khripkov, A., Ilvonen, J., van Wonterghem, J., & Viikari, V. (2021). Dual-Polarized mm-Wave End-Fire Chain-Slot Antenna for Mobile Devices. *IEEE Transactions on Antennas and Propagation*, 69(1), 25-34. Article 9119206. <https://doi.org/10.1109/TAP.2020.3001434>

---

This material is protected by copyright and other intellectual property rights, and duplication or sale of all or part of any of the repository collections is not permitted, except that material may be duplicated by you for your research use or educational purposes in electronic or print form. You must obtain permission for any other use. Electronic or print copies may not be offered, whether for sale or otherwise to anyone who is not an authorised user.

# Dual-Polarized mm-Wave Endfire Chain-Slot Antenna for Mobile Devices

Resti Montoya Moreno<sup>b</sup>, Joni Kurvinen<sup>b</sup>, Juha Ala-Laurinaho<sup>b</sup>,  
Alexander Khripkov<sup>b</sup>, *Member, IEEE*, Janne Ilvonen<sup>1b</sup>, Jari van Wousterghem,  
and Ville Viikari<sup>b</sup>, *Senior Member, IEEE*

**Abstract**—This article describes a dual-polarized endfire antenna array for millimeter-wave (mm-wave) frequencies. The antenna consists of a chain-slot-shaped pattern on a mobile phone metal frame. The antenna is fed using a transmission line, which would cause only a negligible capacitive loading of the sub-6 GHz antenna realized on the same metal frame and, therefore, would not significantly degrade its performance. This makes colocating the sub-6 GHz and mm-wave antennas in the same, shared volume possible. Measurements indicate that a four-element array placed within a mobile phone provides a realized gain between 8 and 12.6 dBi for both polarizations across the entire band from 24.5 to 29.5 GHz. The total efficiency of a single element is better than  $-2$  and  $-3$  dB for the whole band for horizontal and vertical polarizations, respectively.

**Index Terms**—5G, antenna, beamsteering, endfire antenna array, metallic rim, millimeter-wave (mm-wave) frequencies, mobile phone.

## I. INTRODUCTION

**F**UTURE 5G mobile devices will use millimeter-wave (mm-wave) bands (such as those at 24–80 GHz) concurrently with the currently used sub-6 GHz bands for increased data rates [1]–[3]. However, many unresolved challenges remain, especially in mobile mm-wave antennas. First, the volume reserved for all the antennas in a mobile device is very limited, and the added mm-wave antennas should be ideally accommodated in the same shared volume with the sub-6 GHz antennas. Additional volume reserved for antennas would otherwise make the mobile device larger and bulkier and, thus, less attractive to customers. Currently, known mm-wave antennas either require additional volume or, if placed in the same volume, significant changes in the design of the

sub-6 GHz antennas in order to avoid major performance degradation.

The mobile device can be in almost any orientation relative to the access point in its normal use, making electrical beamsteering necessary. The mm-wave antennas should additionally be dual-polarized for increased capacity and reliability. Commonly used mm-wave antennas realized on a printed circuit board (PCB) support radiation in the broadside directions of the mobile device [4]. However, they do not easily radiate toward the edges of the phone. Dual-polarized operation can also be relatively easily achieved in broadside direction using, for instance, dual-polarized patch antennas [5], [6]. On the other hand, dual-polarized antennas radiating toward the edges are much more demanding to implement with the commonly used PCB technology. This is, in particular, because the thickness of the PCB is small compared with the wavelength. Therefore, implementing antennas, such as dipoles or other radiating structures, where the electric field is perpendicular to the PCB is challenging.

The mm-wave antennas, similar to sub-6 GHz antennas, should be compliant with the phone design, and they should not introduce changes that result in significant degradations of the visual appearance, robustness, or manufacturability of the device. The majority of mobile devices currently have a metal frame surrounding the device for robustness and esthetic reasons. The metal frame makes directing mm-waves to edge directions very demanding, as any antenna placed inside the frame is obscured by the metal in the endfire direction.

The mm-wave (endfire) antennas have attracted a lot of attention recently [7]–[21]. However, the presented antennas generally have a relatively narrowband, or they operate only with a single polarization. Furthermore, the volume reserved for the mm-wave antenna may be relatively large [22], or the metal frame, which would heavily impact the performance of the antennas, is not included.

Other prior solutions are incompatible with sub-6 GHz antennas due to the very close proximity of the antennas to the metal frame, where the sub-6 GHz antennas are realized. Due to the close distance, the mm-wave antenna significantly loads the sub-6 GHz antennas, deteriorating its operation. Moreover, the mm-wave antenna may be impractical due to multiple gaps and slots needed in the metal frame, such as in [23]. The coexistence between long-term evolution (LTE) and mm-wave antennas in different environments has recently

Manuscript received January 7, 2020; revised April 19, 2020; accepted June 3, 2020. Date of publication June 16, 2020; date of current version January 5, 2021. This work was supported by Huawei Technologies Finland. The work of Joni Kurvinen was supported in part by the Aalto ELEC Doctoral School, in part by the Finnish Foundation for Technology Promotion, and in part by the Nokia Foundation. (*Corresponding author: Resti Montoya Moreno.*)

Resti Montoya Moreno, Joni Kurvinen, Juha Ala-Laurinaho, and Ville Viikari are with the Department of Electronics and Nanoengineering, School of Electrical Engineering, Aalto University, 00076 Espoo, Finland (e-mail: resti.montoyamoreno@aalto.fi).

Alexander Khripkov, Janne Ilvonen, and Jari van Wousterghem are with Huawei Technologies Finland, 00180 Helsinki, Finland.

This article has supplementary downloadable material available at <https://ieeexplore.ieee.org>, provided by the authors.

Color versions of one or more of the figures in this article are available online at <https://ieeexplore.ieee.org>.

Digital Object Identifier 10.1109/TAP.2020.3001434



Fig. 1. mm-wave module may be disguised as speaker slots that are already present in smartphones, such as the Huawei P9.

been studied in some article. Kurvinen *et al.* [24] combined LTE and mm-wave endfire operation, but the proposed antenna array only operates at a single polarization, and beamsteering capabilities are only demonstrated in the  $\pm 25^\circ$  range. In [25], excellent efficiency is achieved in the 24.75–27.5 GHz band, but the metal frame is not included, and the beamsteering capabilities are not presented. In [26], good performance is achieved in the 26–28.5 GHz band, including high realized gain, but the mm-wave antennas present only single polarized broadside operation. In [27], a dual-polarized mm-wave antenna operating at 30 GHz is presented. In this solution, the mm-wave antenna is 1 mm offset from the metal frame, and thus, it is not integrated into it. Moreover, this solution requires the addition of a fairly large rectangular window in the metal frame in order to achieve an endfire radiation pattern, which may not be visually appealing.

In comparison with the previously presented antennas, the proposed design provides the following benefits.

- 1) Sub-6 GHz and mm-wave antennas can coexist in a shared volume without significant performance degradation in either of the antennas.
- 2) Shaping of the metal frame may be similar to current microphone/speakers grill slots, such as those shown in Fig. 1. This makes the design esthetically attractive and acceptable.
- 3) The antenna is integrated into the metal frame, and therefore, this solution is compatible with any metal-frame phone design.
- 4) The presented solution supports independent beamsteering at two polarizations.
- 5) This solution provides a large angular coverage range in the endfire direction, making it easy to achieve full-sphere coverage with complementing broadside antennas.
- 6) The presented solution makes possible feeding the mm-wave antenna elements on the metal frame from the main body without short-circuiting the metal frame or significantly loading it capacitively at sub-6 GHz frequencies.
- 7) The feeding can be realized on a simple PCB together with the mm-wave module and the mm-wave excitation elements coupling to the aperture.

This article presents an endfire mm-wave antenna array implemented in a metal-framed mobile phone structure. The mobile phone structure resembles the one of the modern smartphones where a metal frame is generally present, and the clearance



Fig. 2. Chain-slot antenna concept on a metal frame.

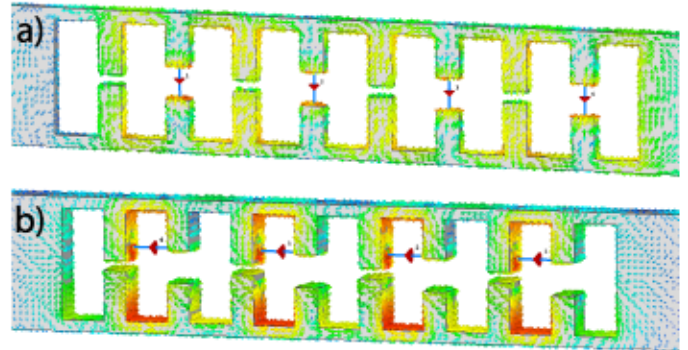


Fig. 3. Surface current distribution at 28 GHz for (a) vertical and (b) horizontal polarizations. Simplified structures with lumped ports are shown to explain the basic operation.

between the frame and the main body is generally 1 mm. The mm-wave module is fed using feed lines that do not short-circuit the sub-6 GHz antennas implemented in the metal frame [28]. A prototype is manufactured, and the performance of each antenna is measured and compared with the corresponding simulated results in order to validate the presented antenna concept.

In Section II, we describe the mm-wave antenna concept and its corresponding feeding structure alongside with the main antenna dimensions. Section III presents the main considerations taken into account when manufacturing the prototype. Simulation and measurement results are analyzed and compared in Section IV. Parametric sweeps and explanations for the differences between measured and simulated results are included in Section V. Finally, conclusions are given in Section VI.

## II. mm-WAVE CHAIN-SLOT ANTENNA CONCEPT, FEEDING STRUCTURE, AND LOW-BAND ANTENNA

### A. Chain-Slot Antenna Concept

The chain-slot antenna array consists of two main parts: a patterned slot in the metal frame and separate coupling elements for both polarizations. The pattern in the metal frame comprises multiple slots interlaced with each other, creating an aperture structure resembling a silhouette of a chain (see Fig. 2). Therefore, the antenna is referred to as a chain-slot antenna. The chain-like slot is patterned so that it supports structural resonance modes at two different polarizations, enabling the use of the slot as a dual-polarized antenna with proper feed structures. The feed elements can be realized on a PCB and are, therefore, relatively easy and inexpensive to manufacture. The chain-like patterned slot on the metal frame can be filled with a dielectric material, such as plastic, for robustness and sealing purposes.

Figs. 3 and 4 show the surface current and  $E$ -field distribution for the chain-slot concept at 28 GHz in a simplified

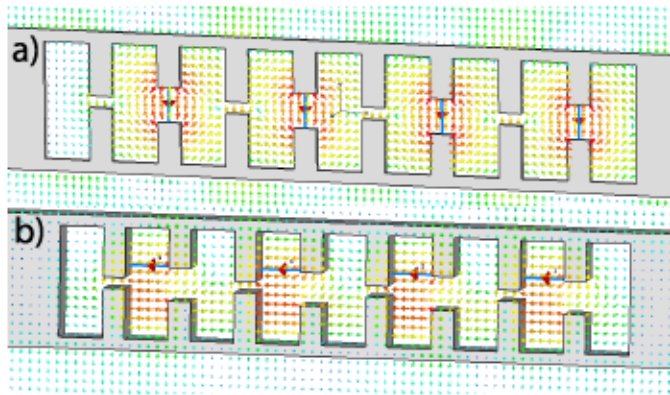


Fig. 4. Electric field distribution at 28 GHz for (a) vertical and (b) horizontal polarizations. Simplified structures with lumped ports are shown to explain the basic operation.

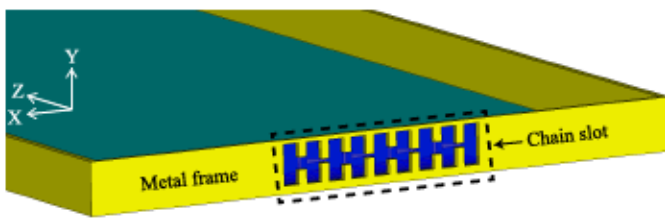


Fig. 5. Antenna front view (outside the mobile device).

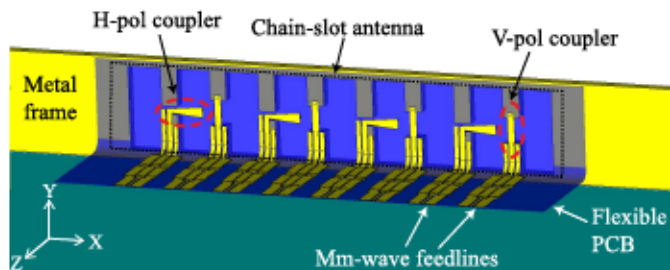


Fig. 6. Chain-slot antenna back view (seen from inside the phone). The metallic unibody of the phone is hidden to avoid shadowing of the antenna.

structure. This structure is fed with ideal lumped ports for simplicity. As seen in the figures, both horizontally and vertically polarized fields are generated when the structure is fed. In practice, coupling elements must be included in order to excite the desired modes. Moreover, the coupling elements exhibit another resonance, which leads to a double-resonance operation. The front view of the chain-slot antenna implemented on the metal frame of a mobile phone is shown in Fig. 5. The coupling elements for exciting the horizontal and vertical (H-Pol and V-Pol, respectively) polarizations are shown in Fig. 6. The vertical polarization is excited by creating a voltage difference across the narrow part of the chain-slot pattern with an extended signal line of a coplanar waveguide, whereas the horizontal polarization is excited using a monopole-shaped planar probe. The pattern repeats periodically depending on the number of the elements in the array, and one coupling element mainly excites one period of the slot pattern. The combination of the coupling element and the chain-slot aperture in the metal frame forms a multiresonant

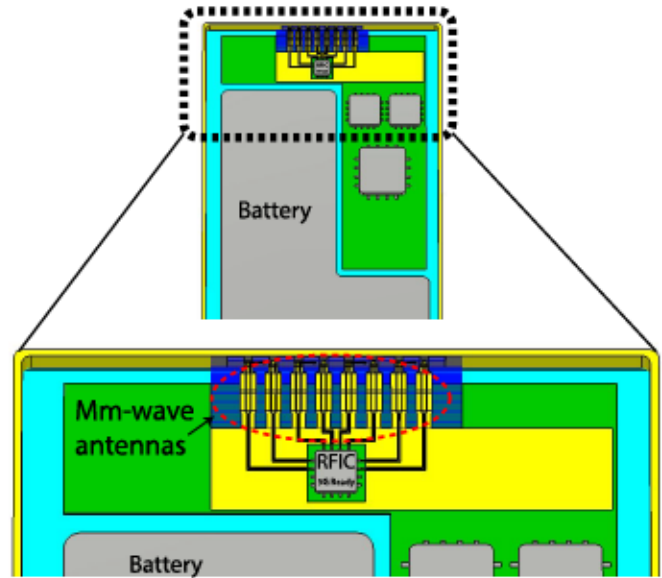


Fig. 7. mm-wave antenna connection with the RFIC inside the smartphone.

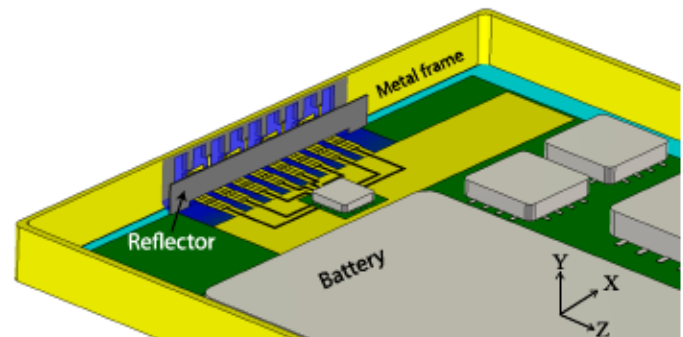


Fig. 8. mm-wave antenna connection with the RFIC, including a vertically oriented reflector that has been hidden in Figs. 6 and 7 for visualization purposes.

structure, enabling a wide impedance band. This solution is based on shaping the metal frame. Modern smartphones use the metal frame as a part of the sub-6 GHz antennas. However, the proposed shaping does not introduce gaps for the currents and has a very small effect on the performance of the sub-6 GHz antennas.

Fig. 7 shows the chain-slot concept implemented in a modern smartphone. The coupling elements may be fed from an RFIC 5G transceiver module placed near it. In addition, the battery or other element already present in the phone can be used as a back-reflector behind the slot to direct energy outwards. If this is not possible due to the phone layout, an additional reflector (e.g., a thin, vertically oriented metal sheet) can be used, as shown in Fig. 8. This reflector has been hidden in the previous figures for visualization purposes.

To simplify the manufacturing process of the antenna prototype, we realize both the unibody and the metal cover of the phone on the same PCB, supplemented with one additional 3-D-shaped metal part acting as a reflector. As shown in Fig. 9, both the bent model and the prototyped planar structure follow the same operational principle. The only difference between

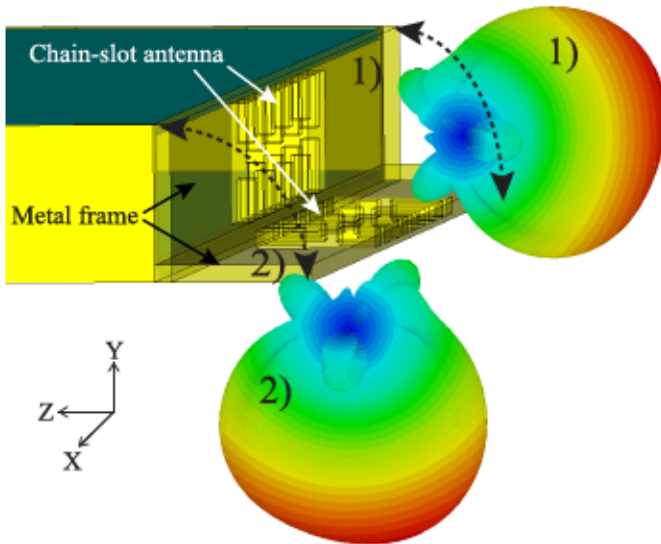


Fig. 9. Chain-slot antenna. 1: conventional mobile phone model where radiation is directed toward the edge of the phone. 2: prototyped structure in a planar form where radiation is directed toward the back side of the phone.

both models is the direction of the radiation. Section III explains the prototype structure in more detail. The dimensions and results shown in Sections III–V of this article correspond to the planar, prototyped structure.

### B. Feeding Structure for mm-Wave Antennas

One common way of realizing sub-6 GHz antennas on metal-frame phones is using capacitive coupling elements (CCEs) [29], where a part or section of the metal frame is used as the antenna element. It is important that the coupling element is separated from the main conductive body (ground) of the device with a gap. Generally, the larger the gap between the metal frame and the main body, the better the sub-6 GHz antenna performance (especially below 1 GHz [30]). The main drawback with currently known mm-wave antennas for metal-frame mobile devices is that they short-circuit the metal frame or significantly load the CCE capacitively. Capacitive loading effectively decreases the gap between the CCE antenna and the main body and, thus, degrades the operation of the antenna. In other solutions, such as in [31], the metal frame is galvanically shorted, which deteriorates the performance of the sub-6 GHz antenna. In [32], an mm-wave antenna integrated with a microstrip filter is presented. However, the coupled-line filter shorts the metal frame through the ground plane, thus altering the low-band antenna performance.

An mm-wave transmission line that introduces low common-mode capacitance not degrading sub-6 GHz antenna operation is presented in [28]. This transmission line does not significantly load the sub-6 GHz antennas and is, thus, called electrically invisible. The invisibility is achieved by minimizing the common-mode capacitance of the line, i.e., the capacitive loading between the metal frame and the main conductive body. In practice, the capacitance is minimized by introducing series capacitances or gaps in the transmission line, both in the signal and ground conductors in the case of an unbalanced line and on both conductors in the case of a

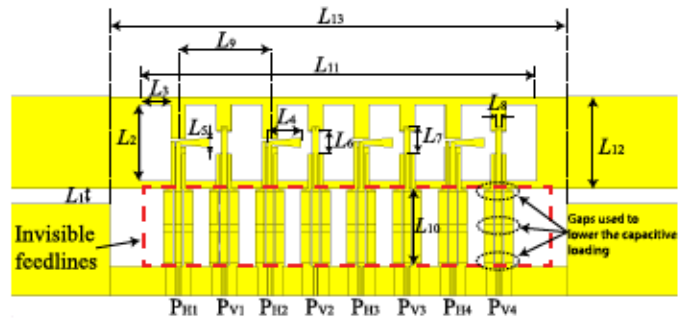


Fig. 10. Chain-slot antenna and invisible feed.  $P_{Hi}$  and  $P_{Vi}$  refer to horizontal and vertical polarizations, where  $i$  is the element number.

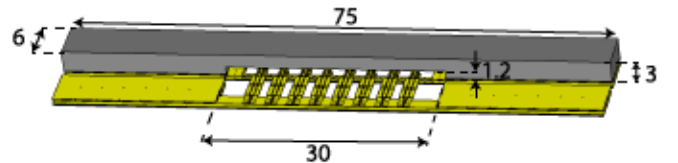


Fig. 11. Reflector with the main dimensions in mm.

balanced line. The larger the gaps, the smaller the common mode capacitance, and the less the line loads the sub-6 GHz antennas. The series capacitance at mm-wave frequencies is compensated with series or parallel inductances or both so that the mm-wave signal can propagate along the line without significant attenuation. The appropriate series inductances can be realized with short transmission line sections of approximately a quarter of the wavelength. Conventionally designed high-pass or bandpass filters are not suitable to deliver the mm-wave signal to the antenna element. This is because the filter theory considers the same wave mode for the pass and stop bands. In this case, a high-pass filter causes a high reflection of the differential mode propagating in the line. However, the differential mode is not as important as the sub-6 GHz antenna only experiences the common-mode loading due to the mm-wave feed line.

In the proposed design, we use the electrically invisible feed line that is presented, in detail, in [28]. Fig. 10 shows both the feeding structure and the mm-wave antenna array. The reflector that is hidden for visualization purposes in the previous figure is shown in Fig. 11.

## III. PROTOTYPE CONSIDERATIONS

A prototype is manufactured to verify the concepts presented in Section II. For the sake of simplicity, the prototype is manufactured on a PCB of size  $156 \times 75 \times 0.96 \text{ mm}^3$ . The required PCB consists of six metal layers and five substrate layers with different thicknesses and relative permittivities ranging between 3.12 and 3.35, as shown in Fig. 12. The core material has  $\tan \delta = 0.003$ , whereas the remaining dielectrics have  $\tan \delta = 0.002$ . The main chain-slot dimensions in Table I are for the dimensions in Fig. 10. The prototype consists of the connectors, the feeding lines (GCPW), the invisible feed lines, and the chain-slot antenna, as shown in Fig. 13. Due to the size of the connectors, they are placed in two rows on the PCB such that the H-pol connectors are placed closer

TABLE I  
MAIN DIMENSIONS OF THE CHAIN-SLOT ANTENNA

| Dimension | Description                            | Value (mm) |
|-----------|--|------------|
| $L_1$     | Metal-frame to ground-plane clearance  | 1          |
| $L_2$     | Slot height                            | 5          |
| $L_3$     | Slot width                             | 2          |
| $L_4$     | Horizontal polarization coupler length | 2.2        |
| $L_5$     | Horizontal polarization coupler width  | 0.2-0.6    |
| $L_6$     | Vertical polarization slot length      | 1.5        |
| $L_7$     | Vertical polarization coupler length   | 1.75       |
| $L_8$     | Vertical polarization coupler width    | 0.4        |
| $L_9$     | Inter-element spacing                  | 6          |
| $L_{10}$  | Invisible feedline module length       | 5          |
| $L_{11}$  | mm-wave antenna array length           | 26         |
| $L_{12}$  | Metal frame height                     | 6          |
| $L_{13}$  | mm-wave cut-out                        | 30         |

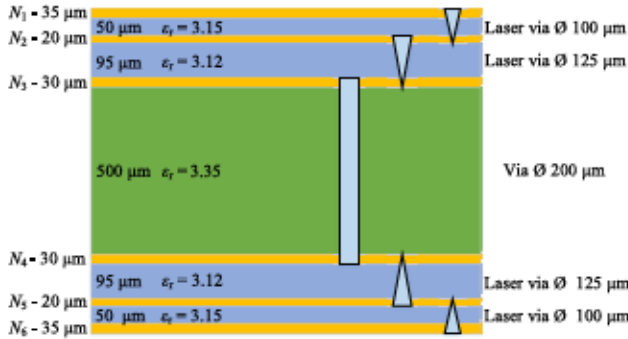


Fig. 12. PCB stack-up of the manufactured prototype.

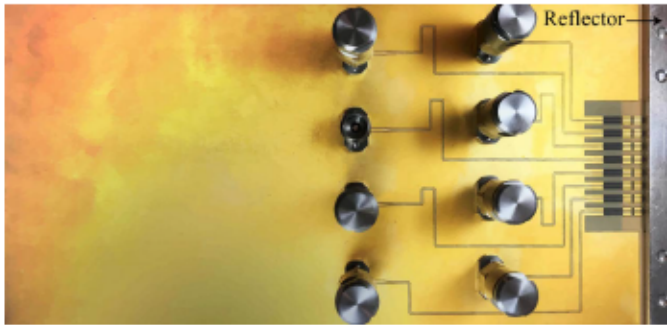


Fig. 13. Prototyped PCB.

to the antenna. As shown in Fig. 13, an aluminum reflector is screwed to the metal frame at a distance of 1.2 mm from the antenna. Fig. 14 shows a close-up of the top part of the prototype, where the invisible feed lines and the H-pol and V-pol couplers are implemented.

Since the primary goal of the prototype is to verify that the proposed concept performs as expected, a planar structure is used, which greatly simplifies the manufacturing process. As a result, the radiated energy is directed toward the broadside of the PCB. The mm-wave feed lines and significant fields are between the thin copper layers N1–N3, and by using a flexible PCB, these feed lines could be bent, making the antenna radiate toward endfire direction.

The metal-frame shaping is done in layers N3–N6 of the PCB, and the different layers are interconnected using multiple vias, making its electrical behavior similar to that of a solid metal structure.

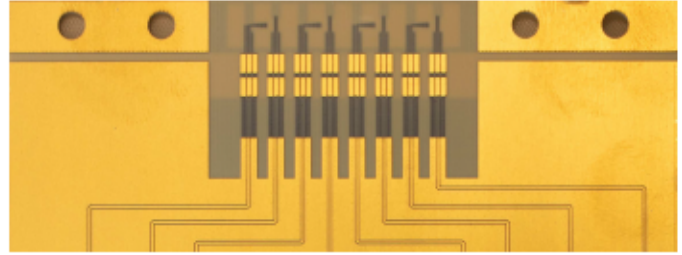


Fig. 14. Top side of the prototyped chain-slot antenna without the reflector.

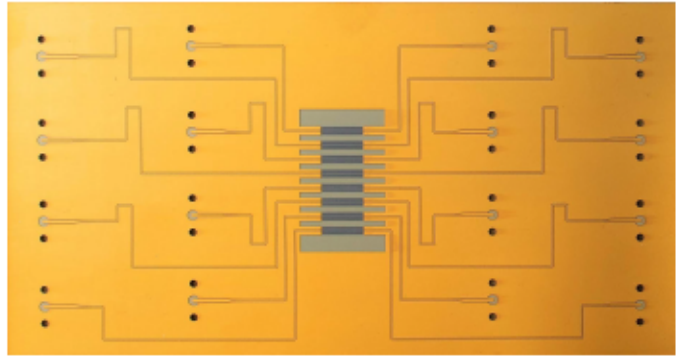


Fig. 15. Prototyped test board used to measure the introduced insertion loss of the transmission lines to each port.

#### IV. mm-WAVE MEASUREMENT RESULTS

In order to evaluate the antenna and the invisible feed line performance, the losses in the connectors and transmission lines must be compensated. Therefore, the additional test board shown in Fig. 15 is manufactured. The test board allows us to determine the insertion loss at each port with great precision via transmission measurements.

Due to the available measurement setup, each antenna port is measured individually. The four-element array results have been obtained by combining the individually measured, port-specific radiation patterns computationally in MATLAB. The beamsteered array patterns have been calculated by adding a phase shift between the individually measured antenna patterns. All the results presented in this article have been loss-compensated with the reference plane located at the beginning of the invisible feed line. This way, the invisible feed lines are part of the studied antenna structure.

The 2.4 mm female compression mount connectors are used to feed each of the eight antennas. When measuring the performance of a single antenna element, the remaining ports are terminated in 50  $\Omega$  loads.

The measured and simulated reflection coefficients for horizontally and vertically polarized antennas are shown in Figs. 16 and 17, respectively. Matching levels are mostly below  $-10$  dB for the simulated S-parameters in the 24.5–29.5 GHz range. However, the measured S-parameters present a frequency shift, and the matching levels achieved for the vertically polarized antennas are generally higher than those predicted by simulations. The possible reasons for these differences are explained in Section V. Both horizontally and vertically polarized arrays display dual-polarized operation

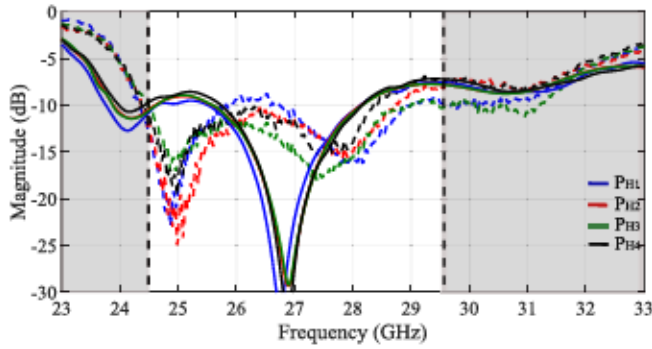


Fig. 16. Reflection coefficient of the chain-slot antenna for the horizontally polarized antennas. Solid lines: simulated values. Dashed lines: measured ones.

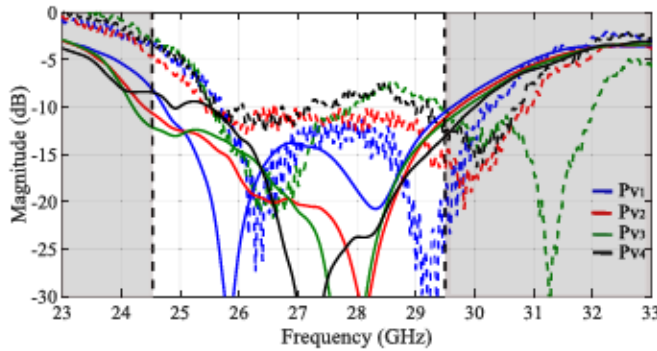


Fig. 17. Reflection coefficient of the chain-slot antenna for the vertically polarized antennas. Solid lines: simulated values. Dashed lines: measured ones.

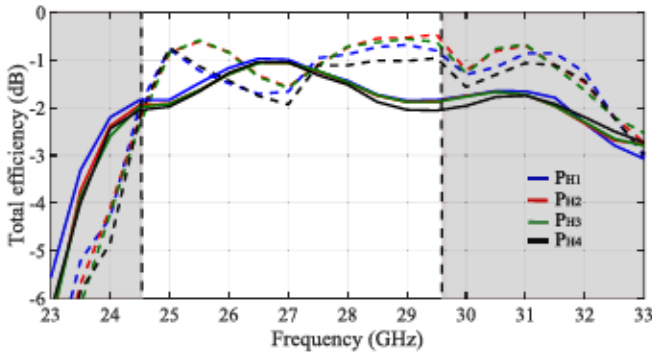


Fig. 18. Measured and simulated total efficiency for H-pol antennas. Solid lines: simulated values. Dashed lines: measured ones.

corresponding to the chain-slot and feeding-element modes. The coupling between differently polarized ports is  $-15$  dB at worst and, generally, well below  $-20$  dB.

Figs. 18 and 19 compare the simulated and measured total efficiencies for horizontal and vertical polarizations, respectively. The simulated efficiency is generally below the measured level. A possible reason for this would be an over compensation of the used surface roughness in the simulations ( $0.6 \mu\text{m}$ ).

Fig. 20 shows the measured and simulated peak realized gain for the four-element arrays. Measured realized gain is above  $8$  dBi for both polarizations, and the peaks are at

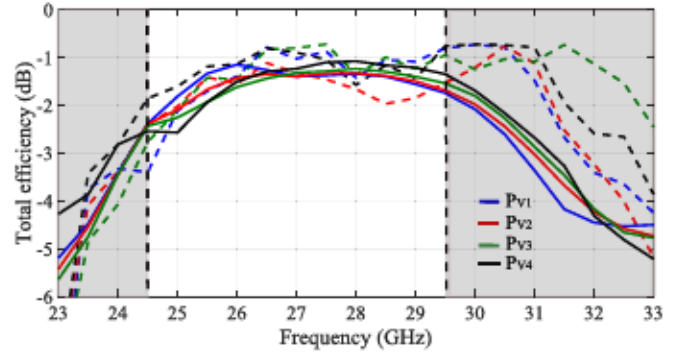


Fig. 19. Measured and simulated total efficiency for V-pol antennas. Solid lines: simulated values. Dashed lines: measured ones.

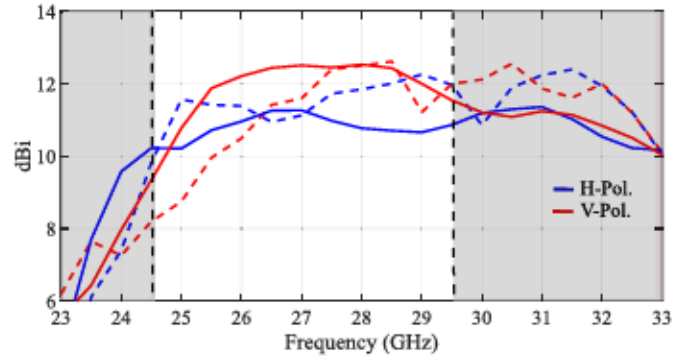


Fig. 20. Measured and simulated peak realized gain for the four-element arrays. Solid lines: simulated values. Dashed lines: measured ones.

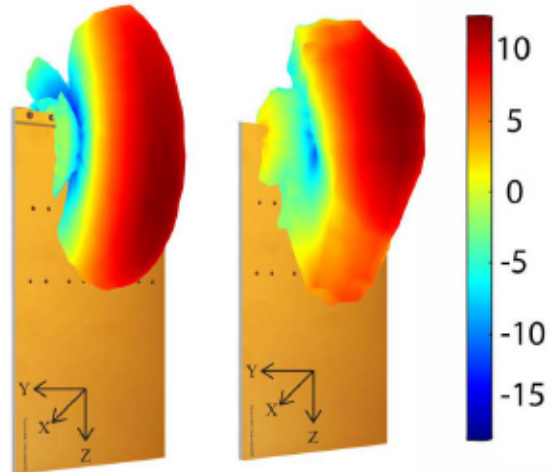


Fig. 21. Measured and combined 3-D radiation pattern of the four-element array at  $28$  GHz for H-pol and V-pol, respectively. Values are in dBi.

$12.6$  and  $12.3$  dBi for the vertical and horizontal polarizations, respectively. Fig. 21 shows the measured and combined 3-D boresight radiation patterns for the four-element arrays for the horizontal and vertical polarizations. Since 3-D coverage is a key feature in mm-wave antenna arrays, beamsteering capabilities are of crucial importance. Figs. 22 and 23 show the beamsteering capabilities of the four-element array at  $28$  GHz. Beamsteering up to  $\pm 50^\circ$  is possible with a scan loss below  $3$  dB for horizontal polarization and  $\pm 40^\circ$  for

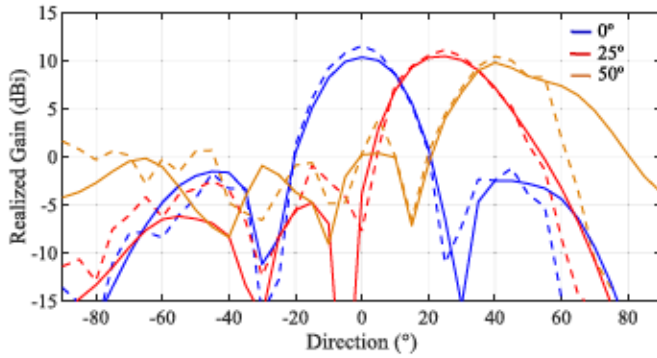


Fig. 22. Realized gain-radiation pattern of the chain-slot antenna array at 28 GHz for horizontal polarization. Solid lines: simulated values. Dashed lines: measured ones.

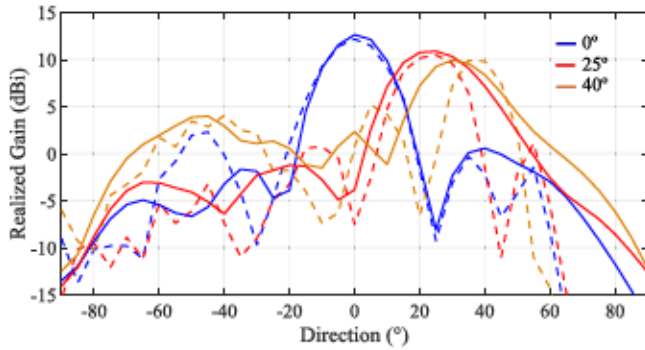


Fig. 23. Realized gain-radiation pattern of the chain-slot antenna array at 28 GHz for vertical polarization. Solid lines: simulated values. Dashed lines: measured ones.

vertical polarization. For the horizontal polarization, there is an almost perfect agreement between the simulated and measured beamsteering performance. The difference between the measured and simulated patterns when steering up to  $\pm 50^\circ$  is due to the measurement setup, where part of the radiation was blocked when approaching the  $+75^\circ$  limit. Differences between the simulated and measured patterns for the vertical polarization are slightly more noticeable. The authors believe that this could be caused by the manual placement of the vias, which is explained in detail in Section V. The measured beamsteering capability at the edges of the operation band, i.e., at 24.5 and 29.5 GHz, is comparable to that shown at 28 GHz. However, the results are not shown for conciseness.

## V. ANALYSIS OF RESULTS AND TOLERANCE STUDY

This section strives to explain the differences between the simulated and measured results, as well as provides indicators on how to recover from these differences in order to achieve the desired performance.

### A. Horizontally Polarized Array

The simulated and measured results are generally in good agreement for the horizontally polarized antennas. Efficiency, realized gain, and beamsteering capabilities do not differ by more than 1 dB. However, there is a systematic 700 MHz frequency shift between the measured and simulated S-parameters. The frequency shift can be explained by a small

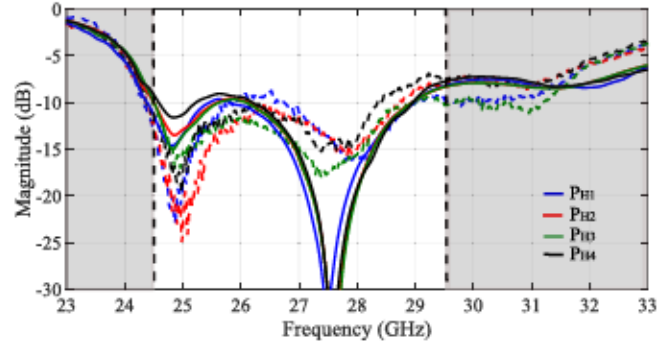


Fig. 24. Reflection coefficient of the chain-slot antenna for the horizontally polarized antennas. Solid lines: simulation results with modified permittivity and surface roughness values. Dashed lines: measured ones.

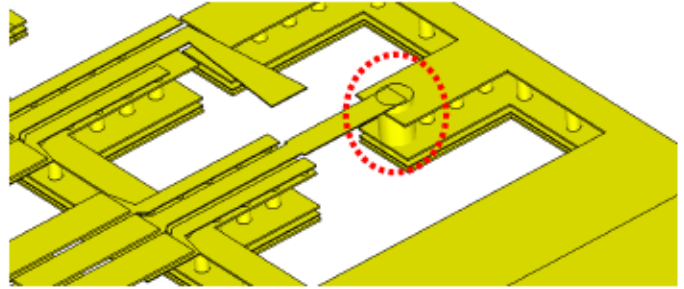


Fig. 25. Shunt via for vertically polarized antennas.

change in the relative permittivities of the dielectrics used in the PCB. Moreover, Fig. 16 shows that the simulated efficiency is slightly lower than the measured one. This may indicate that the surface roughness used in simulations was slightly too high. Furthermore, decreasing the roughness contributes to the increase in the resonant frequency of the array. Fig. 24 shows the measured and simulated S-parameters for the horizontally polarized array when the permittivity of the dielectric is modified from the original 3.35 to 3.1 and the roughness from 0.6 to  $0.1 \mu\text{m}$ . An almost perfect agreement between the resonant frequencies of the simulated and measured values is observed in this figure. Simulations show that the primary dimensions affecting the two resonances are the probe length ( $L_4$  in Fig. 9) and the aperture dimensions ( $L_2$  and  $L_3$  in Fig. 9). Both the feeding elements and the chain-slot structures are strongly coupled, and therefore, modifying one of the two will affect both resonances.

### B. Vertically Polarized Array

Evaluating the differences between the measured and simulated S-parameters for the vertically polarized antennas clearly indicates that there are more differences than just a simple frequency shift. While the frequency shift is still apparent here, the bandwidth and resonances achieved are different.

During the last part of the simulation phase, a via critical to the performance of the vertically polarized antennas was found (see Fig. 25). The diameter of this via had to be at least 0.5 mm. However, manufacturing reasons restricted the maximum diameter to 0.2 mm. This problem was solved by replacing the 0.2 mm via with a 0.5 mm through via by drilling

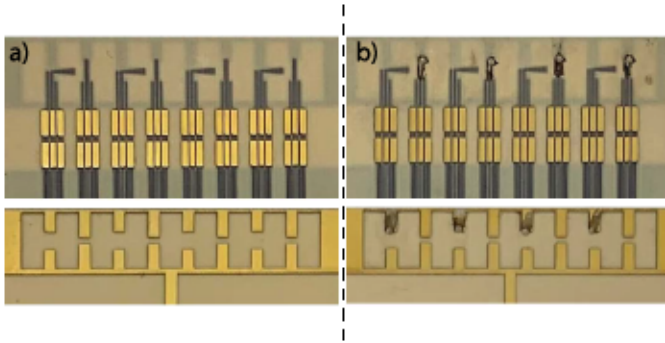


Fig. 26. (a) Prototyped chain-slot antenna. (b) Modified version with shunt via added manually.

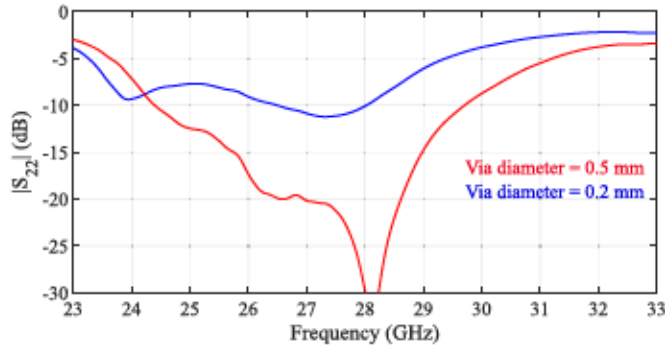


Fig. 27. Reflection coefficient of the chain-slot antenna for port P2 of the vertically polarized antennas for two via diameters.

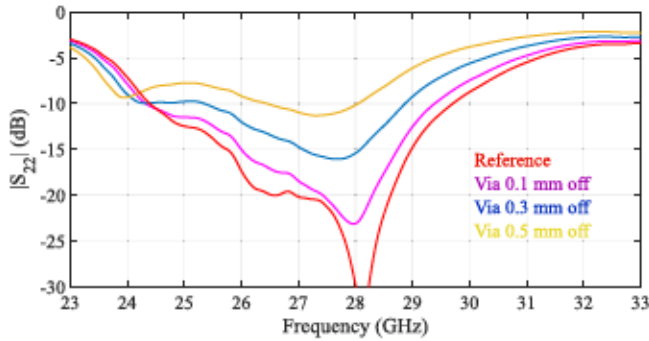


Fig. 28. Reflection coefficient of the chain-slot antenna for port P2 of the vertically polarized antennas.

a 0.5 mm hole and then filling it with a silver-based PDS material. This process was done manually for each of the four vias, which results in increased uncertainty in the performance. Fig. 26 shows the initially prototyped PCB on the left and the later modified PCB with the added via on the right. Fig. 27 shows different performances achieved for two via diameters.

Fig. 28 shows a parametric sweep of the via location in the vertical direction. This sweep shows that the via location has a significant effect on the reflection coefficient level. Although the sweep shows the difference in performance when the via is misplaced in the vertical axis, a horizontal misalignment is also possible in reality. From the measurement results, we believe that the via corresponding to port P1 was the one done with the highest precision, followed by the ones

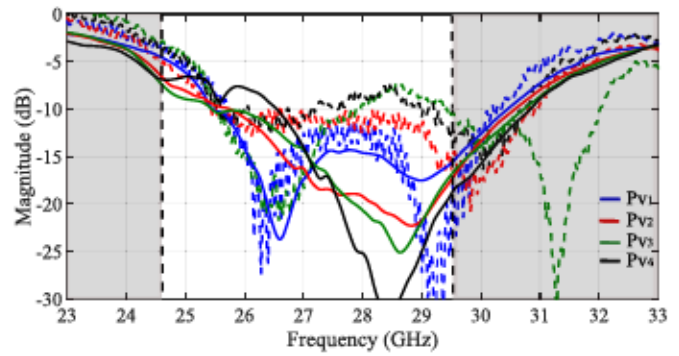


Fig. 29. Reflection coefficient of the chain-slot antenna for the vertically polarized antennas. Solid lines: simulation results with modified permittivity and surface roughness values. Dashed lines: measured ones.

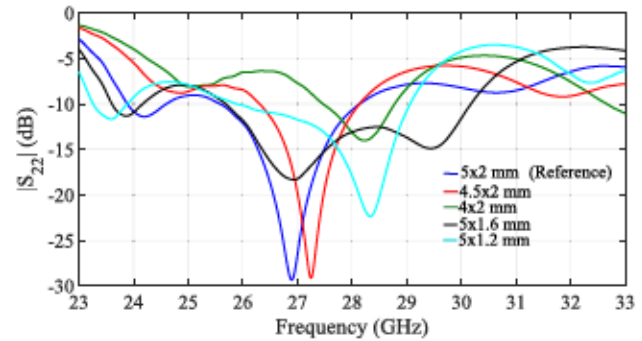


Fig. 30. Reflection coefficient of the chain-slot antenna for port P2 of the horizontally polarized antennas for different  $L_2$  and  $L_3$  dimensions.

in ports 2, 4, and, finally, 3. On the other hand, determining precisely how accurately the manually made vias were located is very difficult. However, the authors believe that this will not be a problem in a real product since the metal frame is made out of solid metal instead of vias.

Fig. 29 shows the S-parameters for the vertically polarized antennas when the permittivity and surface roughness values are adjusted to 3.1 and  $0.1 \mu\text{m}$ , respectively. A rather good agreement is achieved for ports P1 and P2. For these results, the via size and location have not been modified with respect to the reference model. For these antennas, the main dimensions determining the resonances are the distance between the two poles of the chain slot ( $L_6$  in Fig. 9), the aperture dimensions ( $L_2$  and  $L_3$  in Fig. 9), and the V-pol probe dimensions ( $L_7$  and  $L_8$  in Fig. 9). Sometimes, the two resonances are so close to each other that they add up, showing as a single resonance.

### C. Tolerance Analysis

In this section, we sweep the dimensions  $L_2$  and  $L_3$  (dimensions of one subslot) since they are the most relevant for both polarizations. Figs. 30 and 31 present the reflection coefficient for the middle port P2 for horizontal and vertical polarizations, respectively, and show how it varies with different dimensions. For the horizontal polarization, small changes in  $L_2$  result in a frequency offset in the resonant frequency, while more drastic changes also result in a detuned structure, deteriorating the reflection coefficient.  $L_3$  is also very critical for the

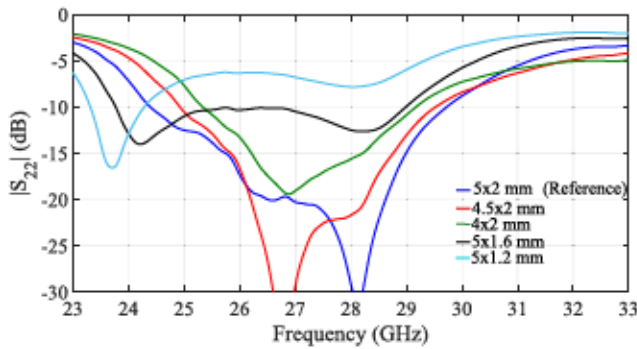


Fig. 31. Reflection coefficient of the chain-slot antenna for port P2 of the vertically polarized antennas for different  $L_2$  and  $L_3$  dimensions.

performance of this polarization, affecting the bandwidth and resonance level achieved. For the vertical polarization,  $L_2$  seems to have an effect on the resonance frequency, while  $L_3$  affects its strength (matching level). The dimensions  $L_2$  and  $L_3$  need to be chosen to provide the best tradeoff between the operations at both polarizations.

VI. CONCLUSION

This article presents a 5G mm-wave phased-array mobile-phone antenna that is implemented in the metal frame. The dual-polarized operation with an efficiency higher than  $-3$  dB in the 24.5–29.5 GHz range is demonstrated. The realized gain of the mm-wave array is above 8 dBi over the entire frequency band. The beamsteering range of at least  $\pm 40^\circ$  is possible with a scan loss below 3 dB. The mm-wave design shows not only excellent dual-polarized performance but also an appealing appearance to the users since the necessary modifications to current smartphones may be tolerable.

The presented antenna type, if placed on all the edges of the phone, could alone provide the necessary angular and polarization coverage in the 28 GHz band while being able to coexist with the LTE antennas. This makes the solution a very promising candidate for future mobile devices using the mm-wave bands.

ACKNOWLEDGMENT

The authors would like to thank Dr. Anu Lehtovuori, Dr. Jari-Matti Hannula, and Rasmus Luomaniemi for useful discussions and comments. They would also like to thank Sanna Keskiniva for her help with Fig. 21.

REFERENCES

[1] *View on 5G architecture (Version 2.0)*, 5G PPP Archit. Working Group, Berlin, Germany, 2017.  
 [2] *5G Spectrum*, Public Policy Position, Huawei, Shenzhen, China, 2018.  
 [3] *Looking ahead to 5G*, Nokia, Espoo, Finland, 2014.  
 [4] M. Khalily, R. Tafazolli, P. Xiao, and A. A. Kishk, "Broadband mm-wave microstrip array antenna with improved radiation characteristics for different 5G applications," *IEEE Trans. Antennas Propag.*, vol. 66, no. 9, pp. 4641–4647, Sep. 2018.  
 [5] J.-K. Du *et al.*, "Dual-polarized patch array antenna package for 5G communication systems," in *Proc. 11th Eur. Conf. Antennas Propag. (EUCAP)*, Mar. 2017, pp. 3493–3496.

[6] H. Xia, T. Zhang, L. Li, and F.-C. Zheng, "A low-cost dual-polarized 28 GHz phased array antenna for 5G communications," in *Proc. Int. Workshop Antenna Technol. (iWAT)*, Mar. 2018, pp. 1–4.  
 [7] H.-C. Huang, Y. Wang, and X. Jian, "Novel integrated design of dual-band dual-polarization mm-wave antennas in non-mm-Wave antennas (AiA) for a 5G phone with a metal frame," in *Proc. Int. Workshop Antenna Technol. (iWAT)*, Mar. 2019, pp. 125–128.  
 [8] Y. Wang, H.-C. Huang, and X. Jian, "Novel design of a dual-band 5G mm-wave antenna array integrated with a metal frame of a cellular phone," in *Proc. Asia-Pacific Microw. Conf. (APMC)*, Nov. 2018, pp. 1582–1584.  
 [9] M. M. Samadi Taheri, A. Abdipour, S. Zhang, and G. F. Pedersen, "Integrated millimeter-wave wideband end-fire 5G beam steerable array and low-frequency 4G LTE antenna in mobile terminals," *IEEE Trans. Veh. Technol.*, vol. 68, no. 4, pp. 4042–4046, Apr. 2019.  
 [10] R. Rodriguez-Cano, S. Zhang, K. Zhao, and G. F. Pedersen, "Reduction of main beam-blockage in an integrated 5G array with a metal-frame antenna," *IEEE Trans. Antennas Propag.*, vol. 67, no. 5, pp. 3161–3170, May 2019.  
 [11] W. Hong, K.-H. Baek, and S. Ko, "Millimeter-wave 5G antennas for smartphones: Overview and experimental demonstration," *IEEE Trans. Antennas Propag.*, vol. 65, no. 12, pp. 6250–6261, Dec. 2017.  
 [12] J. Zhang, K. Zhao, L. Wang, S. Zhang, and G. F. Pedersen, "Dual-polarized phased array with end-fire radiation for 5G handset applications," *IEEE Trans. Antennas Propag.*, vol. 68, no. 4, pp. 3277–3282, Apr. 2020.  
 [13] N. Ojaroudiparchin, M. Shen, and G. F. Pedersen, "Design of vivaldi antenna array with end-fire beam steering function for 5G mobile terminals," in *Proc. 23rd Telecommun. Forum Telfor (TELFOR)*, Nov. 2015, pp. 587–590.  
 [14] S. Zhang, X. Chen, I. Strytsin, and G. F. Pedersen, "A planar switchable 3-D-coverage phased array antenna and its user effects for 28-GHz mobile terminal applications," *IEEE Trans. Antennas Propag.*, vol. 65, no. 12, pp. 6413–6421, Dec. 2017.  
 [15] N. O. Parchin, M. Shen, and G. F. Pedersen, "End-fire phased array 5G antenna design using leaf-shaped bow-tie elements for 28/38 GHz MIMO applications," in *Proc. IEEE Int. Conf. Ubiquitous Wireless Broadband (ICUWB)*, Oct. 2016, pp. 1–4.  
 [16] N. Ojaroudiparchin, M. Shen, and G. F. Pedersen, "Wide-scan phased array antenna fed by coax-to-microstriplines for 5G cell phones," in *Proc. 21st Int. Conf. Microw., Radar Wireless Commun. (MIKON)*, May 2016, pp. 1–4.  
 [17] W. Hong, K. Baek, Y. Lee, and Y. Geon Kim, "Design and analysis of a low-profile 28 GHz beam steering antenna solution for future 5G cellular applications," in *IEEE MTT-S Int. Microw. Symp. Dig.*, Jun. 2014, pp. 1–4.  
 [18] R. Rodriguez-Cano, S. Zhang, and G. F. Pedersen, "Beam-steerable multi-band mm-wave bow-tie antenna array for mobile terminals," in *Proc. 12th Eur. Conf. Antennas Propag. (EuCAP)*, 2018, pp. 1–4.  
 [19] C. Bartlett, S. S. Hesari, and J. Bornemann, "End-fire substrate integrated waveguide beam-forming system for 5G applications," in *Proc. 18th Int. Symp. Antenna Technol. Appl. Electromagn. (ANTEM)*, Aug. 2018, pp. 1–4.  
 [20] V. Raghavan, M.-L. Chi, M. A. Tassoudji, O. H. Koymen, and J. Li, "Antenna placement and performance tradeoffs with hand blockage in millimeter wave systems," *IEEE Trans. Commun.*, vol. 67, no. 4, pp. 3082–3096, Apr. 2019.  
 [21] J. Bang and J. Choi, "A SAR reduced mm-wave beam-steerable array antenna with dual-mode operation for fully metal-covered 5G cellular handsets," *IEEE Antennas Wireless Propag. Lett.*, vol. 17, no. 6, pp. 1118–1122, Jun. 2018.  
 [22] R. M. Moreno, J. Ala-Laurinaho, and V. Viikari, "Rod waveguides as future 5G antennas for mobile devices," in *Proc. 48th Eur. Microw. Conf. (EuMC)*, Sep. 2018, pp. 1081–1084.  
 [23] B. Yu, K. Yang, C.-Y.-D. Sim, and G. Yang, "A novel 28 GHz beam steering array for 5G mobile device with metallic casing application," *IEEE Trans. Antennas Propag.*, vol. 66, no. 1, pp. 462–466, Jan. 2018.  
 [24] J. Kurvinen, H. Kahkonen, A. Lehtovuori, J. Ala-Laurinaho, and V. Viikari, "Co-designed mm-wave and LTE handset antennas," *IEEE Trans. Antennas Propag.*, vol. 67, no. 3, pp. 1545–1553, Mar. 2019.  
 [25] Z. Ren, S. Wu, and A. Zhao, "Coexist design of sub-6GHz and millimeter-wave antennas for 5G mobile terminals," in *2018 Int. Symp. Antennas Propag. (ISAP)*, Oct. 2018, pp. 1–2.

- [26] R. Hussain, A. T. Alreshaid, S. K. Podilchak, and M. S. Sharawi, "Compact 4G MIMO antenna integrated with a 5G array for current and future mobile handsets," *IET Microw., Antennas Propag.*, vol. 11, no. 2, pp. 271–279, Jan. 2017.
- [27] R. M. Moreno, J. Ala-Laurinaho, A. Khripkov, J. Ilvonen, and V. Viikari, "Dual-polarized mm-Wave end-fire antenna for mobile devices," *IEEE Trans. Antennas Propag.*, early access, Apr. 30, 2020, doi: 10.1109/TAP.2020.2989556.
- [28] J. Kurvinen *et al.*, "Capacitively-loaded feed line to improve mm-wave and sub-6 GHz antenna co-existence," *IEEE Access*, to be published.
- [29] J. Kurvinen, A. Lehtovuori, J. Mai, C. Wang, and V. Viikari, "Metal-covered handset with LTE MIMO, Wi-Fi MIMO, AND GPS antennas," *Prog. Electromagn. Res. C*, vol. 80, pp. 89–101, Jan. 2018.
- [30] J. Ilvonen, R. Valkonen, J. Holopainen, and V. Viikari, "Design strategy for 4G handset antennas and a multiband hybrid antenna," *IEEE Trans. Antennas Propag.*, vol. 62, no. 4, pp. 1918–1927, Apr. 2014.
- [31] J. Park, S. Y. Lee, Y. Kim, J. Lee, and W. Hong, "Hybrid antenna module concept for 28 GHz 5G beamsteering cellular devices," in *IEEE MTT-S Int. Microw. Symp. Dig.*, Aug. 2018, pp. 1–3.
- [32] I. Syrytsin, M. Shen, and G. F. Pedersen, "Antenna integrated with a microstrip filter for 5G mm-wave applications," in *Proc. Int. Conf. Electromagn. Adv. Appl. (ICEAA)*, Sep. 2018, pp. 438–441.



**Resti Montoya Moreno** was born in Albacete, Spain, in 1992. He received the B.Sc. (Tech.) degree in telecommunications engineering from the Universitat Politècnica de València, Valencia, Spain, in 2014, and the M.Sc. (Tech.) degree (Hons.) in electrical engineering from Aalto University, Espoo, Finland, in 2016, where he is currently pursuing the D.Sc. (Tech.) degree.

He was a Research Assistant with Aalto University before joining Intel as an RF Engineer Intern in 2016. His current research interests include 5G and mm-wave antennas for base stations and mobile devices.



**Joni Kurvinen** was born in Espoo, Finland, in 1991. He received the B.Sc. (Tech.) and M.Sc. (Tech.) (Hons.) degrees in electrical engineering from Aalto University, Espoo, in 2014 and 2016, respectively, where he is currently pursuing the D.Sc. (Tech.) degree with the Department of Electronics and Nanoengineering, School of Electrical Engineering.

In 2016, he was a Research Assistant with Aalto University. His current research interests include handset antennas and antenna coexistence in 5G and MIMO systems.



**Juha Ala-Laurinaho** received the Diploma Engineer (M.Sc.) degree in mathematics and the D.Sc. (Tech.) degree in electrical engineering from the TKK Helsinki University of Technology, Espoo, Finland, in 1995 and 2001, respectively.

He has been with the TKK Helsinki University of Technology. He served in the Radio Laboratory from 1995 to 2007, in the Department of Radio Science and Engineering from 2008 to 2016, and currently serves in the Department of Electronics and Nanoengineering, Aalto University. Currently,

he works as a Staff Scientist. He has been a Researcher and Project Manager in many millimeter-wave technology-related projects. His current research interests are the antennas and antenna measurement techniques for millimeter and submillimeter waves, and the millimeter-wave imaging.



**Alexander Khripkov** (Member, IEEE) received the B.S. degree in radio engineering and the Ph.D. degree in antennas and microwave devices from the Southern Federal University of Russia, Rostov-on-Don, Russia, in 2002 and 2007, respectively.

From 2007 to 2012, he was a Researcher with the Department of Ultrawide Band Sensors for Medical Applications, Industrial Technology Research Institute, Taiwan. From 2012 to 2016, he was a Group Leader of the Electromagnetic Solutions Group, Samsung R&D Institute, Moscow, Russia. He is currently a Principal Antenna Engineer with the Terminal Antenna and RF Lab, Huawei Technologies Finland, Helsinki, Finland. He has authored or coauthored about 30 articles in peer-reviewed journals and conference proceedings, holds eight granted U.S. patents and about 20 granted patents in other countries. His current research interests include microwave/millimeter-wave antennas and circuits, millimeter-wave systems, terminal antennas, reconfigurable antenna arrays, metamaterial-inspired structures.

Dr. Khripkov was a recipient of over ten industrial awards. He serves as a reviewer for more than 20 journals in the IEEE Antennas and Propagation Society and the *IET Communications*.



**Janne Ilvonen** was born in Helsinki, Finland, in 1976. He received the M.Sc. and Lic.Sc. degrees (Hons.) and the D.Sc. (Tech.) degree in electrical engineering from Aalto University, Aalto, Finland, in 2009, 2012, and 2014, respectively.

From 2015 to 2016, he was a Senior Antenna Engineer with Microsoft Mobile, Espoo, Finland, where he was developing antenna concepts for Microsoft's future flagship handsets. Since 2016, he has been with Huawei Technologies Finland, Helsinki, as a Principal Antenna Engineer. His current research interest includes sub-6 GHz and mm-wave 5G handset antennas.



**Jari Van Wonerghem** received the Engineering (B.Sc.) degree in radio technology from the Kymenlaakso Institute of Applied Science, Kouvolaa, Finland, in 1999.

From 1999 to 2009, he was a Senior Antenna Engineer with Nokia Mobile Phones in Finland and Canada. From 2009 to 2011, he was a Senior Antenna Engineer with Blackberry. After returning to Finland in 2011, he joined Nokia Mobile Phones again as a Senior Antenna Specialist. From 2016 to 2019, he was with Huawei Technologies, Helsinki, Finland, as a Principal Antenna Engineer. He is currently a Principal Antenna Engineer with Radientum, Tampere, Finland. His recent activities include 5G sub-6 GHz antenna and 5G mm-wave antenna array designs, and their effective integration into commercial products.



**Ville Viikari** (Senior Member, IEEE) was born in Espoo, Finland, in 1979. He received the Master of Science (Tech.) and Doctor of Science (Tech.) degrees (Hons.) in electrical engineering from the Helsinki University of Technology (TKK), Espoo, in 2004 and 2007, respectively.

He is currently an Associate Professor and the Deputy Head of department with the Aalto University School of Electrical Engineering, Espoo. From 2001 to 2007, he was with the Radio Laboratory, TKK, where he studied antenna measurement techniques at submillimeter wavelengths and antenna pattern correction techniques.

From 2007 to 2012, he was a Research Scientist and a Senior Scientist with the VTT Technical Research Centre, Espoo, where his research included wireless sensors, RFID, radar applications, MEMS, and microwave sensors. His current research interests include antennas for mobile networks, RF-powered devices, and antenna measurement techniques.

Dr. Viikari was a recipient of the Young Researcher Award of the year 2014 presented by the Finnish Foundation for Technology Promotion, the IEEE Sensors Council 2010 Early Career Gold Award, the 2008 Young Scientist Award of the URSI XXXI Finnish Convention on Radio Science, Espoo, Finland, and the Best Student Paper Award of the Annual Symposium of the Antenna Measurement Techniques Association, Newport, RI, USA (October 30–November 4, 2005). He has served as the Chair of the Technical Program Committee of the ESA Workshop on Millimetre-Wave Technology and Applications and the Global Symposium on Millimeter Waves (GSMM) twice, in 2011 and 2016, in Espoo.